Vortex Dynamics and Spectra Fluctuations in a Superfluid Disk

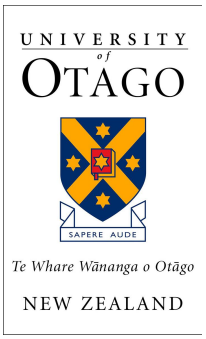

Michael Cawte

Department of Physics
University of Otago

This dissertation is submitted for the degree of
Bachelor of Science with Honours in Physics

September 2016

Declaration

I hereby declare that except where specific reference is made to the work of others, the contents of this dissertation are original and have not been submitted in whole or in part for consideration for any other degree or qualification in this, or any other university. This dissertation is my own work and contains nothing which is the outcome of work done in collaboration with others, except as specified in the text and Acknowledgements.

Michael Cawte
September 2016

Acknowledgements

I would like to acknowledge my supervisor Ashton Bradley. I very much enjoyed working with him on this project and the sense of adventure shared while exploring different mathematical models and physical phenomena. I gained valuable insight from him into how to characterise the properties of a new physical system, tease apart the individual elements and make well justified simplifying assumptions to uncover the underlying physics.

I would like to thank Mathew Reeves, his help has been invaluable and I would not have learned anywhere near as much as I have without him. He spent many hours with me bug hunting, discussing my project and physics in general. I feel fortunate to have a friend whom I can share my enthusiasms with.

I would also like to thank Craig Chisholm and Jelena Rakonjac, for pointing out obvious bugs to me in the early hours of the mornings, shared proof readings and making light of mistakes. I would also like to acknowledge the camaraderie and banter in the honours room throughout the year. Everyone has been a pleasure to work with.

And thanks to James Boocock, who taught me the importance of working hard. His tales of working 100 hour weeks during his masters thesis were intimidating and grimly motivating. Who knew that talking about genetics at the pub with colleagues counted towards working hours.

Thanks to Herschel for making me take you for walks. It was good to have a reason to get outside. And finally my to wife Jennifer, for putting up with the late nights and dry explanations of my project. You are still beautiful despite all the broken sleep I have caused you.

Abstract

The macroscopic dipole fluctuations of two clusters of vortices in a circular domain is investigated. An analytic solution for two vortices in the domain is first derived by perturbation, giving a prediction on the frequency of the dipole oscillation and aspect ratio of the elliptical trajectory. Simulations of dipolar clusters comprised of many vortices were done to check the analytic predictions. The dipole fluctuation spectra as a function of energy was explored, finding good agreement with our analytical result over a broad range of system energies, particularly at high energy.

Table of contents

Chapter 1

Introduction

Vortices are a feature of many physical phenomena, from neutron stars [1] to turbulent flows, to tornados to the bathtub. In classical fluids they occur in regions where the fluid particles have an angular momentum, with the fluid often expelled from the centre of rotation. Vortices also exist in more exotic phases of matter, such as plasmas [2], degenerate quantum gasses [3] and superfluids[4]. The physical characteristics of vortices in a superfluid are distinct from those in a classical fluid. Vortices in a classical fluid can decay by diffusion, whereas vortices in a superfluid occur in an inviscid flow. The superfluid vortices have quantized circulation [5] rather than continuous circulation and the core of the vortices are much smaller than their classical counterparts.

In this project the vortex dynamics of superfluid helium in a complex condensed matter system are investigated. The motivation for this project is to build a model of an experiment conducted at the University of Queensland [6]. The experimenters set out to create an enhanced optomechanical micro-toriodial resonator by using helium as a photo-convective superfluid to enhance the radiation pressure used to drive the resonator. By preparing a 2μm thick silicon wafer with a layer of silicon dioxide and using photolithographic methods, a microscopic silicon disk on a raised pedestal can be etched out[7]. During the process of lithography, a CO2 laser melts the rim of the disk into glass, creating a micro-toriodal whispering gallery mode resonator.

The experimental group at the University of Queensland obtained one of these resonators with an inner radius of 3μm and an outer radius of 37.5μm. Figure 1.2 shows a scanning tunnel microscope image of the resonator. The resonator was placed inside a helium-3 cryostat containing low pressure helium-4 gas. The pressure of the gas was selected to ensure that the helium transitioned directly to the superfluid state at a temperature of 1K, bypassing the normal fluid phase [6]. Once the temperature had been lowered below 1K, a thin film of helium-4 coated the resonator and silicon base.

Techniques from cavity optomechanics allow optical degrees of freedom to be coupled to mechanical degrees of freedom in micro-scale mechanical systems. The coupling is achieved in this system by introducing laser light into the micro-toroid via tapered optical fibre, exciting the whispering gallery modes of the resonator.

The radiation pressure of the light can be used to drive mechanical oscillations in the resonator. The Queensland team exploited the properties of the liquid helium to increase the strength of the optomechanical coupling over the radiation pressure alone by an order of magnitude[8]. By using a property of superfluid helium known as the fountain effect, the optical heat created by the laser induces the superfluid helium to travel up the silicon pedestal towards the heat source. Upon reaching the light, the superfluid then evaporates off the side of the resonator imparting an inwards mechanical force.

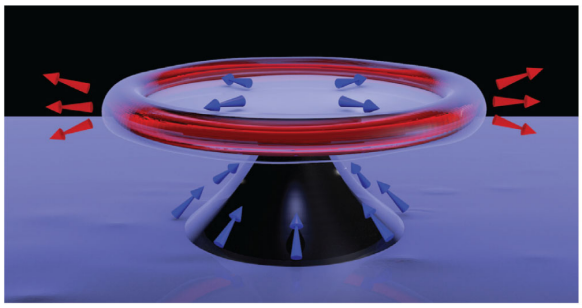

Fig. 1.1 Schematic of photo-convective superfluid motion in the experimental system. The system contains a micro-toroidal optical resonator situated on a pedestal. A thin film of superfluid helium coating the optical device travels up the pedestal, toward a focal point of optical heating via the fountain effect. Figure reproduced from [8].

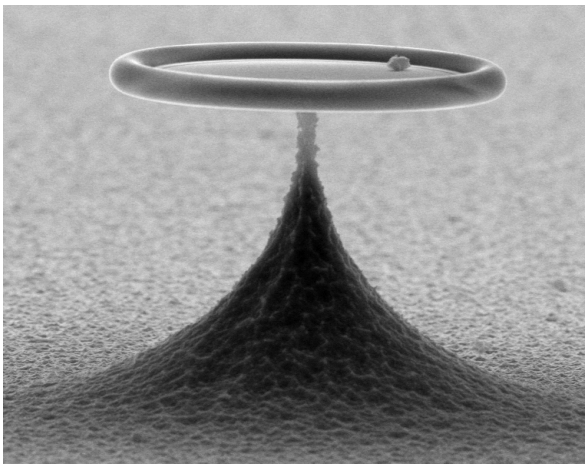

Fig. 1.2 Scanning tunnel microscope image of micro-toriodial resonator. Figure reproduced from [8].

The superfluid that does not evaporate travels into the inner radius of the flat disk on top of the resonator. It is the region of fluid inside this disk that will be modelled to gain understanding of the system.

Chapter 2 provides a background on Cavity Optomechanics, Liquid Helium and fluids in two dimensions. Chapter 3 sets out the physical system and the assumptions of the model. Chapter 4 introduces the point vortex model in the plane and then the bounded circular domain. Chapter 5 gives the results of an analytic treatment of two point vortices in the bounded circular domain. Chapter 6 details the numerical method and defines the units used in numerical simulations. Chapter 7 contains the results of the numerical simulations preformed. Finally, Chapter 8 provides a summary of the project.

Chapter 2

Background

2.1 Cavity Optomechanics

The field of cavity optomechanics studies the interaction between electromagnetic radiation and micro-mechanical motion. Since a photon carries a momentum of $p = \hbar k$ (where k is the wave number), a large number of photons can be used to create a radiation pressure. Precise control over the degrees of freedom of an optical field can be used to excite specific modes of a mirco-mechanical system. A physical system in which there is a coupling between optical and mechanical degrees of freedom is known as an optomechanical system [9].

The simplest optomechanical system to examine is the Fabry-Perot resonator. The resonator contains two mirrors a distance L apart. These mirrors can support resonances of [10]

$$\omega_{cav,m} = \pi \frac{c}{L}, \tag{2.1}$$

where m is the mode number and c is the speed of light. The separation between resonances is given by the free spectral range [10]

$$\Delta\omega_{FSR} = \pi \frac{c}{L}. \tag{2.2}$$

Photons scattering from an atom or molecule is known as Ramen scattering [11]. Raman scattering is the inelastic scattering of a photon and matter. Raman scattering can impart or take away energy from the mechanical vibration of an object. The loss or gain of vibrational energy is described by the Stokes/Anti-Stokes process [12]. In the Stokes process the outgoing photon has a lower frequency than the incoming photon and the vibrational energy is increased. In the Anti-Stokes process the outgoing photon has a higher energy than the incoming photon and the vibrational energy is decreased. A single photon Raman scattering

off an object changes very little mechanical vibration energy. In cavity optomechanics, the Raman scattering effect can become significant by scattering against small objects with a large number of photons. In the case of the Fabry-Perot resonator, the mirrors reflect the photons back and forth greatly increasing the number of photon collisions. The optical finesse gives the average number of round trips a photon makes before decaying. It is defined as [10]

$$\mathcal{F} \equiv \frac{\Delta\omega_{FSR}}{\kappa}, \tag{2.3}$$

where κ is the photon cavity decay rate due to imperfections in mirror transparencies and scattering outside of the cavity. The quality factor of the cavity is defined as

$$Q_{opt} = \frac{\omega_{cav}}{\kappa}. \tag{2.4}$$

A different kind of resonator is known as a whispering gallery mode resonator. Examples of a whispering gallery mode resonators include glass and crystal spheres with a high internal reflection. Photons inside the spheres are reflected back inside the sphere at the inner surface with minimal loss.

In 2005 it was shown that a mirotoroidial resonator could be used as an optical cavity with attractive features [13]. The microtoroid offered the possibility of obtaining a high optical finesse with the ability to couple the optical field to the mechanical modes of the resonator. As the radiation pressure distorts the physical structure of the resonator, the optical path length is changed which shifts the optical resonance frequency, creating an optomechanical coupling. The Queensland team amplified the optomechanical coupling of the microtoroidial resonator by using a photo-convective superfluid [8]. The optical field not only coupled to the mechanical modes, but also the third sound modes of the thin liquid helium film. This coupling may be able to be used to measure the motion of vortices in the superfluid film by looking at the frequency splitting of the optical field [6].

2.2 Superfluid Helium in two dimensions

Cooling Helium-4 down below 4.22K at atmospheric pressure produces a colourless liquid called Helium I. Helium I contracts when cooled and boils when heated, but has a much lower viscosity than what is predicted by classical physics. This low viscosity can only be explained by quantum mechanics, making Helium a quantum fluid [14].

Cooling Helium I down below 2.18K produces Helium II. This transition temperature is called the λ point due to the shape of the phase diagram. Helium II is also a superfluid many

interesting properties. It does not boil but evaporates directly to gas and it has a thermal conductivity hundreds of times more than copper.

In 1941 Landau proposed a phenomenological two fluid model to describe liquid helium II [15]. In this model, the liquid has a normal fluid and super fluid component, each with it's own density and velocity. At the λ temperature, the fluid is composed solely of the normal component and at zero temperature only the superfluid component remains. The ratio of normal fluid to superfluid decreases linearly from the λ point to zero temperature.

Landau derived his equations of motion for Helium II by using Galileo's relativity principle and the relevant conservation laws (mass and density)[16]. At sufficiently low velocities, the equations of motion that result are in the form of Euler's equation of an ideal fluid for the superfluid component (2.5), and the incompressible form of the Naiver-Stokes equation for the normal vicious component (2.6) [17]

$$\frac{\partial \mathbf{u_s}}{\partial t} + (\mathbf{u_s} \cdot \nabla)\mathbf{u_s} = \frac{-\nabla P}{\rho_s}, \tag{2.5}$$

$$\frac{\partial \mathbf{u_n}}{\partial t} + (\mathbf{u_n} \cdot \nabla)\mathbf{u_n} - \nu\nabla^2\mathbf{u_n} = \frac{-\nabla P}{\rho_n}, \tag{2.6}$$

where $\mathbf{u_s}$ and $\mathbf{u_s}$ are the superfluid and normal fluid velocity, P is the pressure, ν is the kinematic viscosity and ρ_s a d ρ_n are the superfluid and normal fluid density. The thermal properties of helium II add a thermomechanical term, $\rho_s ST$ to the equations of motion [17].

$$\rho_s \frac{\partial \mathbf{u_s}}{\partial t} = -\frac{\rho_s}{\rho}\nabla p + \rho_s S\nabla T + \frac{\rho_s\rho_n}{2\rho}\nabla(\mathbf{u_n} - \mathbf{u_s})^2 - \mathbf{F_{ns}}, \tag{2.7}$$

$$\rho_s \frac{\partial \mathbf{u_s}}{\partial t} = -\frac{\rho_s}{\rho}\nabla p + \rho_s S\nabla T + \frac{\rho_s\rho_n}{2\rho}, \nabla(\mathbf{u_n} - \mathbf{u_s})^2 - \mathbf{F_{ns}} + \eta\nabla^2\mathbf{u_n} \tag{2.8}$$

where η is the dynamic viscosity and $\mathbf{F_{ns}}$ is the mutual friction between the normal and superfluid components. These two equations can be linearised to obtain velocities for first and second sound. First sound is a propagation of pressure, with the normal and superfluid components moving in phase. In second sound heat takes the place of pressure and the components move out of phase. This is what allows superfluid helium to have its remarkable thermal properties, giving it the highest known thermal conductivity of any material.

Superfluid films form naturally on surfaces owing to the combination of ultra-low viscosity and attractive Van der Waals forces [6]. To first approximation third sound in a thin film has the normal component remaining at rest and a surface wave propagating through the superfluid component [18] .

In 1938, Laszlo Tisza published a paper also using a two fluid model, but this time it treated the superfluid component as a manifestation of Bose-Einstein condensation [19]. By first looking at a single particle of helium, the quantum version of the Euler equation can be derived. Schrodinger's equation of motion is

$$i\hbar\frac{\partial\psi}{\partial t} = \frac{-\hbar^2}{2m}\nabla^2\psi - V\psi. \tag{2.9}$$

By using the Madelung transformation [20], the wave function is set to $\psi = \sqrt{\rho}\exp i\phi$ where ρ is the density. The probability current $\mathbf{j}$ is given by

$$\mathbf{j} = \frac{i\hbar}{2m}(\psi\nabla\psi^* - \psi^*\nabla\psi) = \frac{\hbar}{m}\rho\nabla\phi. \tag{2.10}$$

Given that the current has the form $\mathbf{j} = \rho\mathbf{u}$, the velocity is then

$$\mathbf{u} = \frac{\hbar}{m}\nabla\phi. \tag{2.11}$$

Onsager showed that the phase of ψ must wind by integer amounts of 2π [5]. This means that

$$\int_c \nabla\phi\cdot d\mathbf{l} = 2\pi n \quad (n = 0,\pm1,\pm2,..). \tag{2.12}$$

Defining $\kappa = h/m$, the fluid circulation around a closed curve C is given by

$$\Gamma_C \equiv \oint_C \mathbf{u}\cdot d\mathbf{l} = \kappa\sigma \quad (\sigma = 0,\pm1,\pm2,..), \tag{2.13}$$

where σ is the vortex charge. The vorticity is given by

$$\omega = (\nabla\times\mathbf{u}). \tag{2.14}$$

To derive the vorticity, note that the phase of a charge ±1 vortex located at the origin is given by

$$\phi = \pm\arctan\left(\frac{y}{x}\right) = \pm\theta, \tag{2.15}$$

for polar angle θ. Then the velocity is given by

$$\mathbf{u} = \frac{\hbar}{m}\nabla\phi = \left(\hat{r}\frac{\partial}{\partial r} + \hat{\theta}\frac{1}{r}\frac{\partial}{\partial\theta}\right)\phi = \pm\frac{\hbar}{mr}\hat{\theta}. \tag{2.16}$$

Since the fluid is confined to a two dimensional plane and the vorticity is defined as a curl of the velocity, only the z component of the vorticity needs to be calculated

$$\omega = (\nabla \times \mathbf{u})_z = (\partial_x \partial_y - \partial_y \partial_x)\phi = 0, \tag{2.17}$$

Hence the fluid is irrotational and vorticity is zero everywhere inside the fluid. However vortices can occur where the density of the fluid is zero.

2.3 Special properties of fluids in two dimensions

Since the fluids that will be modelled are inviscid, incompressible and confined to two dimensions, some useful mathematical simplifications can be used. Let $\mathbf{u} = (u, v, 0)$ be the flow velocity in two dimensions. If

$$\nabla \cdot \mathbf{u} = 0, \tag{2.18}$$

is satisfied then we say the fluid is incompressible. The velocity potential can be defined as ϕ, such that

$$\mathbf{u} = \frac{\hbar}{m} \nabla \phi, \tag{2.19}$$

the gradient of the velocity potential gives the flow velocity. By virtue of the incompressibility of the fluid, the velocity potential satisfies the Laplace equation away from the vortex cores

$$\frac{\hbar}{m} \nabla^2 \phi = 0. \tag{2.20}$$

To visualise the flow of the fluid, each fluid particles trajectory can be plotted as a streamline. The stream function gives the streamlines and is defined by use a vector potential ψ, where

$$\mathbf{u} = \frac{\hbar}{m} (\nabla \times \boldsymbol{\psi}). \tag{2.21}$$

Since the fluid is incompressible and the streamline is always tangent to the velocity vector, the stream function must be give a constant value along the streamline. Since $\mathbf{u} = (u, v, 0)$, the curl of the vector potential implies $\boldsymbol{\psi} = (0, 0, \psi)$. The velocity potential and stream function are related by

$$v = \frac{\hbar}{m}\frac{\partial \phi}{\partial x} = \frac{\hbar}{m}\frac{\partial \psi}{\partial x} \quad u = \frac{\hbar}{m}\frac{\partial \phi}{\partial y} = -\frac{\hbar}{m}\frac{\partial \psi}{\partial y}, \tag{2.22}$$

which are in the same form as the Cauchy-Riemann equations. If a complex function is analytic with complex argument $z = x + iy$ and satisfies the Cauchy-Riemann equations then that function is holomorphic. We then define

$$w(z) = \phi(x,y) + i\psi(x,y), \tag{2.23}$$

as the complex potential of the flow. Then the real part of the complex potential, ϕ is the velocity potential, and the imaginary part, ψ is the stream function. Since w(z) is holomorphic, the complex velocity is given by

$$\frac{dw}{dz} = u - iv. \tag{2.24}$$

These properties allow transformation to the complex plane from the real plane, provided the map is an analytic function. This is useful when the flow is inside a complicated geometry, because the problem can be mapped to a simple geometry.

Chapter 3

Physical system and model

3.1 Physical System

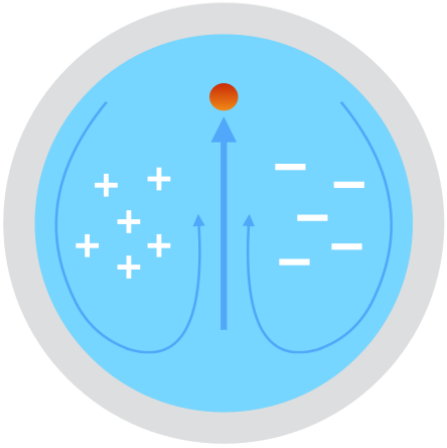

Fig. 3.1 Large-scale dipolar flow about cylindrical defect on top of microtoroidal resonator, causing orientation locking.

3.1.1 Physical System

The system consists of several physical components:

1. *Length scales.*—A thin film of helium consisting of both superfluid and normal fluid. The helium film has been measured to be on the order of $\sim$10nm thick. The size of the disk on top of the torus has a radius of 3.5 μm. The vortex core size is of order

the atomic radius ($\sim 1.5A^o$) [17], and this scale is much smaller than the fluid layer thickness.

2. *Quasi-2D system.*—However, there is significant normal fluid, and the normal fluid is clamped to the surface, providing a significant source of damping. It is expected that the damping will suppress vortex bending, allowing the fluid to be approximated as 2D. The inner wall of the toroid acts as a hard wall boundary for vortex motion, creating a well-defined disk domain for 2D vortex motion.

3. *Superfluid excitations.*—Since the normal fluid is clamped to the surface, the only modes of superfluid excitation are those of *third-sound*, corresponding to phonon excitations of the superfluid moving relative to a stationary normal cloud.

4. *Superfluid forcing.*—Due to the evaporation of helium caused by optical heating on the toroidal perimeter, there is a large flux of superfluid through the system. According to the experimental observations, the flow speed of superfluid through the system is of order $\sim$ 1m/s [8]. Manufacturing defects cause focal points of heating. It is assumed there will be a single dominant point of heating on the toroidal perimeter.

5. *Symmetry breaking.*—A cylindrical defect will cause a symmetry breaking state to emerge with particular orientation locked to the defect.

6. *Steady state.*—Due to the strong forcing and damping, we assume the system involves a quasi-steady state containing many quantum vortices but that it is approximately neutral in net charge, consistent with orientation locking and dipolar flow. We assume the steady-state vortex number is not changing appreciably with time. Such a system will contain significant vortex energy. See Figure 3.1 for a schematic.

7. *Frequency splitting.*—Measurements of frequency splitting between oppositely propagating photons in the mocrotoroid are consistent with a lower bound of 600 vortices on the disk surface [21].

3.2 Motivating the Model

1. A large-scale dipolar flow structure comprised of quantum vortices will couple to the phonon modes of the mechanical oscillator [9]. These vibrational modes in turn generate a signal in the outcoupled light field, a probe of the superfluid dynamics. These vortices may have characteristic dipole moment frequencies of oscillation that are coupled to the mechanical modes of the micro-resonator. By using a point vortex

model in a cylindrically bounded region, the vortex dynamics of this system are modelled and analysed.

2. The optomechanical coupling between the superfluid motion and the mechanical oscillator will be dominated by the large scale motion of the dipolar vortex structure [9]. In this project we focus on understanding the fluctuation spectra of a large-scale vortex dipole.

Chapter 4

Point vortex model

4.1 Point vortices in the plane

In a three dimensional a fluid with vorticity, there are vortex lines that can stretch and tangle into complicated geometrical configurations. Modelling vorticity in three dimensions is a hard numerical problem to solve, which often leads to limiting the area of investigation to a plane perpendicular to all the vortex lines. This limit gives vortices in two dimensions with finite area, greatly reducing complexity. If the fluid is ideal and incompressible with embedded vorticity, a further simplification can be made by using the point vortex model [22].

Since the density of the vortices is low and the core size of the vortices in the thin film of superfluid helium-4 is small relative to the size of the disk on top of the resonator, the vortices can be approximated as points, making the point vortex model an ideal approximation to model the system. So the expression for the vorticity is

$$\omega = (\nabla \times \mathbf{u})_z = \kappa \sum_\alpha \sigma_\alpha \delta^{(2)}(\mathbf{r} - \mathbf{r}_\alpha), \tag{4.1}$$

where $\sigma = \pm 1$ for the sign of the charge. Charges higher than ± 1 are possible, but in practice they are unstable and only charges of ± 1 are relevant in superfluid helium. The stream function is related to the vorticity by Poisson's equation

$$-\Delta\psi(\mathbf{r}) = \omega(\mathbf{r}). \tag{4.2}$$

Now since

$$G(\mathbf{r}) \equiv -\frac{1}{2\pi}\ln|\mathbf{r}|, \tag{4.3}$$

is the Greens solution for a delta function in the plane, then

$$-\Delta G(\mathbf{r}) = \delta^{(2)}(\mathbf{r}). \tag{4.4}$$

The general solution for point vortices is

$$-\Delta\psi(\mathbf{r}) = \kappa\sum_{\alpha}\sigma_{\alpha}G(\mathbf{r}-\mathbf{r}_{\alpha}). \tag{4.5}$$

This leads to the Hamiltonian for vortices in the plane

$$H \equiv \frac{m\rho_0}{2}\int d^2\mathbf{r}|\mathbf{u}|^2, \tag{4.6}$$

Where m and ρ_0 are the mass and density of the superfluid respectively. By expanding out

$$H = \frac{\rho_0}{2}\int d^2\mathbf{r}(\nabla\psi(\mathbf{r}))^2 = \frac{-\rho_0}{2}\int d^2\mathbf{r}\psi(\mathbf{r})\Delta\psi(\mathbf{r}) = \frac{\rho_0}{2}\int d^2\mathbf{r}\psi(\mathbf{r})\omega(\mathbf{r}). \tag{4.7}$$

Kirchoff was the first to show how to state the system in terms of Hamilton's canonical form [23]

$$H = -\frac{\rho_0\kappa^2}{4\pi}\sum_{\alpha}^{N}\sum_{\alpha\neq\beta}^{N}\sigma_{\alpha}\sigma_{\beta}\log\left(\frac{\mathbf{r}_{\alpha}-\mathbf{r}_{\beta}}{\xi}\right). \tag{4.8}$$

where the healing length keeps the log dimensionless. Hamilton's equations in their general form are

$$\dot{q_{\alpha}} = \frac{\partial H}{\partial p_{\alpha}}, \quad \dot{p}_{\alpha} = -\frac{\partial H}{\partial q_{\alpha}}, \tag{4.9}$$

The specific form of Hamilton's equations for the point vortex model are

$$\kappa\sigma_{\alpha}\dot{x}_{\alpha} = \frac{\partial H}{\partial y_{\alpha}}, \qquad \kappa\sigma_{\alpha}\dot{y}_{\alpha} = -\frac{\partial H}{\partial x_{\alpha}}, \tag{4.10}$$

Hence x_{α} and y_{α} are canonically conjugate. The Hamiltonian only has an interaction energy as there is no kinetic energy term since in the point vortex model the vortices have no mass.

Helmholtz was the first to introduce the equations of motion for the point vortex model in 1858 [24]. The vortex equations of motion are

$$\dot{x}_\alpha = \gamma \sum_{\beta \neq \alpha}^{N} \frac{-\sigma_\beta y_{\alpha\beta}}{r_{\alpha\beta}^2}, \qquad \dot{y}_\alpha = \gamma \sum_{\beta \neq \alpha}^{N} \frac{\sigma_\beta x_{\alpha\beta}}{r_{\alpha\beta}^2}, \tag{4.11}$$

where $x_{\alpha\beta} = (x_\alpha - x_\beta)$, $y_{\alpha\beta} = (y_\alpha - y_\beta)$, $r_{\alpha\beta}^2 = x_{\alpha\beta}^2 + y_{\alpha\beta}^2$ and we define a convenient unit of circulation

$$\gamma \equiv \frac{\hbar}{m} = \frac{\kappa}{2\pi}. \tag{4.12}$$

4.2 Bounded Circular Domain

To apply the point vortex model to our system, the boundaries on the disk must be enforced. The method of images can be used to solve the system. If a vortex is placed at position $\mathbf{r}_\alpha$ inside disk of radius R, Then an image vortex placed at

$$\mathbf{r}_\alpha^{\mathbf{im}} = \frac{\mathbf{r}_\alpha R^2}{||\mathbf{r}_\alpha||^2}, \tag{4.13}$$

will ensure that there is no radial velocity on the boundary of the disk. Figure 4.1 shows the arrangement of a positive charged vortex placed inside a disk of radius R and the corresponding negative charged image vortex at the inverse point. The previously used Greens function for the unbounded plane does not satisfied the new boundary condition. An additional term must be added.

$$G_B^{(1)} = \frac{1}{2\pi} \log \left(\frac{R}{||\mathbf{r}_\alpha|| \cdot ||\mathbf{r} - \mathbf{r}_\alpha^{\mathbf{im}}||} \right). \tag{4.14}$$

The total Greens function is now

$$G_T = \frac{1}{2\pi} \left[\log ||\mathbf{r} - \mathbf{r}_\alpha|| - \log \left(\frac{R}{||\mathbf{r}_\alpha|| \cdot ||\mathbf{r} - \mathbf{r}_\alpha^{\mathbf{im}}||} \right) \right]. \tag{4.15}$$

The Hamiltonian is then

$$H = -\frac{\rho_0 \kappa^2}{4\pi} \left[\sum_{\alpha \neq \beta}^{N} \log ||\mathbf{r} - \mathbf{r}_\alpha|| - \sum_{\alpha}^{N} \log \left(\frac{R}{||\mathbf{r}_\alpha|| \cdot ||\mathbf{r} - \mathbf{r}_\alpha^{\mathbf{im}}||} \right) \right]. \tag{4.16}$$

Finally, by using a conformal map, the Hamiltonian and equations of motion are transformed to be in terms of complex position.

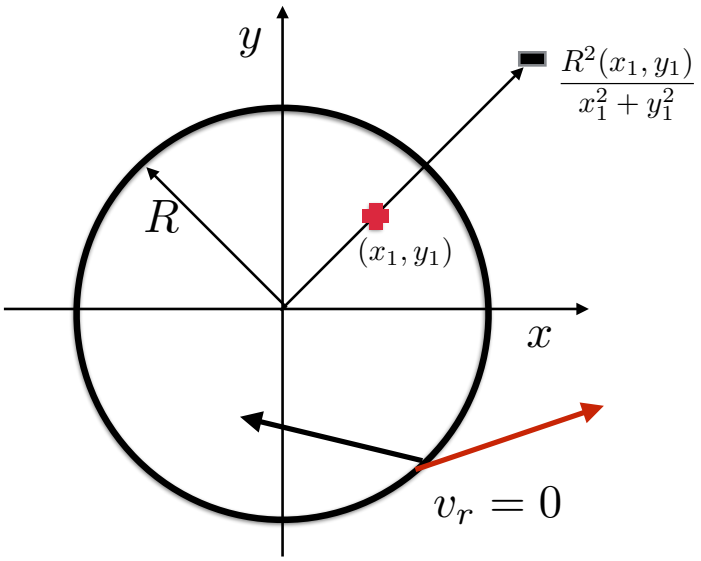

Fig. 4.1 Vortex and Image Vortex

$$H = -\frac{\rho_0 \kappa^2}{4\pi}\left[\sum_{\alpha\neq\beta}^{N} \sigma_\alpha \sigma_\beta \log\frac{||\mathbf{z}_\alpha - \mathbf{z}_\beta||}{|R^2 - \mathbf{z}_\alpha \mathbf{z}_\beta^*|} - \sum_{\alpha}^{N} \sigma_\alpha \log(R^2 - |\mathbf{z}_\alpha|^2)\right]. \tag{4.17}$$

Giving the equation of motion for vortex α as

$$\dot{z}_\alpha^* = -\frac{\rho_0 \kappa^2}{4\pi}\left[\sum_{\alpha\neq\beta}^{N} \frac{\sigma_\beta}{z_\alpha - z_\beta} - \sum_{\alpha}^{N} \frac{\sigma_\beta z_\beta^*}{R^2 - z_\beta^* z_\alpha}\right]. \tag{4.18}$$

Chapter 5

Analytic Results

5.1 Stationary Solution

By exploiting the symmetry of the disk, the equation of motion for only one vortex is needed. A positive vortex is placed at position $z = d$, and a negative vortex at $z = -d$ where the phase is set to zero for both vortices. Setting the phase to zero causes no loss of generality in the results because of the symmetry of the disk.

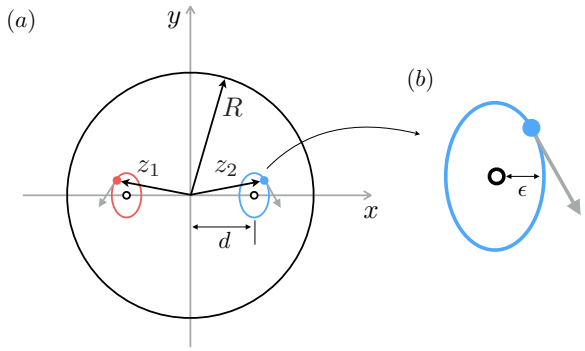

Fig. 5.1 a) Perturbation Schematic: d is the stationary distance from the origin, R is the radius of the disk and z_1 and z_2 mark the positive and negative charged vortex respectively. b) Shows the perturbation of each vortex, where ε is the magnitude of the perturbation.

The equation of motion (4.18) is then used

$$\dot{z}_2^* = -i\gamma\left[\frac{1}{z_2 - z_1} + \frac{z_1^*}{R^2 - z_1^* z_2} - \frac{z_2^*}{R^2 - |z_2|^2}\right] \tag{5.1}$$

By setting the equation of motion equal to zero, the stationary points can be solved for.

$$\frac{1}{z_2 - z_1} + \frac{z_1^*}{R^2 - z_1^* z_2} - \frac{z_2^*}{R^2 - |z_2|^2} = 0 \tag{5.2}$$

$$\frac{1}{2d} - \frac{d}{R^2 + d^2} - \frac{d}{R^2 - d^2} = 0 \tag{5.3}$$

$$d^2 = \frac{-4R^2 + \sqrt{(4r^2)^2 + 4R^2}}{2} \tag{5.4}$$

Solving gives a stationary point of $d^2 = R^2(\sqrt{5} - 2)$, or

$$d = \frac{R}{\phi^{3/2}} \tag{5.5}$$

where $\phi = (1 + \sqrt{5})/2$ is the golden ratio.

5.2 Linear Perturbation

Next the two vortices are perturbed by small amount ε. Initially the perturbation was anticipated to result in circular orbits about the stationary positions but this approach lead to unphysical results. Here we assume that the perturbation will result in elliptical orbits about the stationary positions and we find consistent solutions. The initial equations are

$$z_1 = -d - \varepsilon(e^{i\omega t} - qe^{-i\omega t}) \tag{5.6}$$

$$z_2 = d + \varepsilon(e^{-i\omega t} - qe^{i\omega t}) \tag{5.7}$$

The equation of motion for $\dot{z}_2^* = i\omega\varepsilon(e^{i\omega t} + qe^{-i\omega t})$ is then

$$i\omega\varepsilon(e^{i\omega t}+qe^{i\omega t}) = -i\gamma\left[\frac{1}{(d+\varepsilon(e^{-i\omega t}-qe^{i\omega t}))-(-d-\varepsilon(e^{i\omega t}-qe^{-i\omega t}))}\right.$$
$$-\frac{d+\varepsilon(e^{-i\omega t}-qe^{i\omega t})}{R^2-(d+\varepsilon(e^{-i\omega t}-qe^{i\omega t}))(d+\varepsilon(e^{-i\omega t}-qe^{i\omega t}))}$$
$$\left.-\frac{d+\varepsilon(e^{i\omega t}-qe^{-i\omega t})}{R^2-(d+\varepsilon(e^{-i\omega t}-qe^{i\omega t}))(d+\varepsilon(e^{i\omega t}-qe^{-i\omega t}))}\right] \tag{5.8}$$

We expand and simplify

$$-\frac{\omega\varepsilon}{\gamma}(e^{i\omega t}+qe^{i\omega t}) = \left[\frac{1}{(2d+2\varepsilon\cos\omega t(1-q)}\right.$$
$$-\frac{d+\varepsilon(e^{-i\omega t}-qe^{i\omega t})}{R^2+d^2+2d\varepsilon(e^{-i\omega t}-qe^{i\omega t})}$$
$$\left.-\frac{d+\varepsilon(e^{i\omega t}-qe^{-i\omega t})}{R^2-d^2-2d\varepsilon\cos\omega t(1-q)}\right] \tag{5.9}$$

Since ε is small, we can Taylor expand to first order

$$-\frac{\omega\varepsilon}{\gamma}(e^{i\omega t}+qe^{i\omega t}) = \frac{1}{2d}\left(1-\frac{\varepsilon}{d}(1-q)\cos\omega t\right)-\frac{d+\varepsilon(e^{-i\omega t}-qe^{i\omega t})}{R^2+d^2}\left(1-\frac{2\varepsilon d}{R^2+d^2}(e^{-i\omega t}-qe^{i\omega t})\right)$$
$$-\frac{d+\varepsilon(e^{i\omega t}-qe^{-i\omega t})}{R^2-d^2}\left(1+\frac{2d\varepsilon}{R^2-d^2}(1-q)\cos\omega t\right) \tag{5.10}$$

The stationary solution (5.3) can be identified, eliminating three terms, to give, upon expanding the complex exponentials and dropping the common factor of ε:

$$-\frac{\omega}{\gamma}[(1+q)\cos\omega t+i(1-q)\sin\omega t] = [i(1+q)\sin\omega t-(1-q)\cos\omega t]\frac{R^2-d^2}{(R^2+d^2)^2}$$
$$-[(1-q)\cos\omega t+i(1+q)\sin\omega t]\frac{1}{R^2-d^2}$$
$$-(1-q)\cos\omega t\left(\frac{1}{2d^2}+\frac{2d^2}{(R^2-d^2)^2}\right) \tag{5.11}$$

Identifying the real and imaginary parts gives

$$\frac{\omega}{\gamma} = \frac{(1-q)}{(1+q)}\frac{1}{l_1^2}, \tag{5.12}$$

$$\frac{\omega}{\gamma} = \frac{(1+q)}{(1-q)}\frac{1}{l_2^2}. \tag{5.13}$$

where we define the two convenient length scales

$$\frac{1}{l_1^2} \equiv \frac{R^2-d^2}{(R^2+d^2)^2} + \frac{1}{R^2-d^2} + \frac{1}{2d^2} + \frac{2d^2}{(R^2-d^2)^2} \tag{5.14}$$

$$\frac{1}{l_2^2} \equiv \frac{R^2-d^2}{(R^2-d^2)^2} - \frac{R^2-d^2}{(R^2+d^2)^2}, \tag{5.15}$$

and equating (5.14) with (5.15) we find the aspect ratio of the ellipse

$$\frac{1-q}{1+q} = \frac{l_1}{l_2}, \tag{5.16}$$

and the frequency of orbit

$$\frac{\omega}{\gamma} = \frac{1}{l_1 l_2} \tag{5.17}$$

We can now use properties of the Golden Ratio φ, that satisfies several useful equations, summarised here:

$$\varphi^2-\varphi-1=0, \quad \varphi(\varphi-1)=1, \quad \frac{1}{\varphi}=\varphi-1, \quad 2-\varphi=\frac{1}{\varphi^2}=\frac{1}{\varphi+1}, \quad \varphi=\frac{\varphi+1}{\varphi}, \tag{5.18}$$

Using these properties, we have

$$d^2 = R^2/\varphi^3, \quad R^2-d^2 = 2R^2/\varphi^2, \quad R^2+d^2 = 2R^2/\varphi, \tag{5.19}$$

and we then find the lengths

$$\frac{1}{l_1^2} = \frac{1}{2R^2}(1+\varphi+\varphi^2+\varphi^3) = \frac{1}{2R^2}(3+4\varphi), \quad \frac{1}{l_2^2} = \frac{\varphi}{2R^2}, \tag{5.20}$$

and the aspect ratio

$$\frac{l_1}{l_2} = \sqrt{1+3\varphi} \simeq 2.4195 \tag{5.21}$$

and finally, choosing the unit $\gamma = \hbar/m$ as defined in (4.12), from (5.17) and (5.20) we have frequency

$$\omega = \frac{\hbar}{2mR^2}\sqrt{4+7\varphi} \simeq \frac{\hbar}{mR^2}1.9574. \tag{5.22}$$

In summary, ω is the frequency of dipole oscillations for small amplitude perturbations, and the aspect ratio defines the ratio of the elliptical trajectories the vortices trace out when oscillating around the stationary positions.

Chapter 6

Numerical methods

6.1 Units

The computational simulations of the point vortex model used non-dimensional units. This is done to avoid the computer calculating numbers very large or very small numbers, which would introduce numerical error. The physical variable is denoted by the variable on its own, the dimensionless variable with a bar over top and the characteristic length is given by the variable with a subscript of zero. The variables

$$E = \bar{E}E_0 \quad x_0 = \xi \quad L = \bar{L}L_0 \tag{6.1}$$

define the energy, length and angular momentum. The following choices for the characteristic lengths were made:

$$E_0 = \frac{\rho_0 \hbar}{m} \tag{6.2}$$

$$x_0 = \xi \tag{6.3}$$

where ξ is the healing length of the superfluid. In helium II, the healing length is $\approx 1.5A^o$ [17]. The non-dimensional radius of the disk is also defined in terms of the healing length.

$$R = \bar{R}x_0 = \bar{R}\xi \tag{6.4}$$

The physical radius of the inner disk in the Queensland's team experiment had a radius of $2.5\mu m$. Using the Hellium II healing length gives a non dimensional radius of $\bar{R} \approx 16,666$. The characteristic time scale, t_0, is defined as

$$t_0 = \frac{(\bar{R}\xi)^2 m}{\hbar} \tag{6.5}$$

And angular momentum

$$L_0 = R^2 \rho_0 \kappa \tag{6.6}$$

In what follows, all data is presented in terms of dimensionless variables, unless otherwise stated.

6.2 Numerical model

Mathew Reeves wrote the original code in Matlab for the point vortex model that the simulations were built from. The integration routine used was ode45, with a relative tolerance of 1×10^{-3}. The initial code base was heavily modified, to generate vortex clusters, calculate angular momentum, anneal vortex states and in the later stages of the project the entire code base was changed to use complex positions rather than x and y coordinates.

The simulation represents vortices of positive sign (anti-clockwise rotation) as red points, and vortices of negative sign (clockwise rotation) as blue points. Vortices can be placed in specific positions inside the domain, or they can be generated automatically to preset conditions. In the interests of simplicity and consistency, all simulations had a radius of $\bar{R} = 100$. The macroscopic dipole moment was calculated for each time step in the simulations. This is done by taking the weighted sum of the distance of positive and negative vortices from the origin, and dividing the result by the radius of the disk

$$D = \frac{1}{N} \sum_{\alpha} \kappa_\alpha r_\alpha. \tag{6.7}$$

It is important to understand where the simulation can produce unexpected behaviour. The equations of motion for the point vortex model are

$$\dot{x}_\alpha = \gamma \sum_{\beta \neq \alpha}^{N} \frac{-\sigma_\beta y_{\alpha\beta}}{r_{\alpha\beta}^2}, \qquad \dot{y}_\alpha = \gamma \sum_{\beta \neq \alpha}^{N} \frac{\sigma_\beta x_{\alpha\beta}}{r_{\alpha\beta}^2}, \tag{6.8}$$

where $x_{\alpha\beta} = x_\alpha - x_\beta$, $y_{\alpha\beta} = y_\alpha - y_\beta$, $r_{\alpha\beta}^2 = x_{\alpha\beta}^2 + y_{\alpha\beta}^2$. The point vortex equations are known as a stiff numerical problem. If the inter-vortex distance is very small, the algorithm for the equations of motion is going to compute a very large velocity. If the value of the velocity is too large, the computer will not be able to meet the tolerance requirements of the integration routine and halt. To avoid the simulation halting a softening factor was introduced. This was done by adding 0.0001 to $r_{\alpha\beta}^2$ each time the equations of motion are calculated.

The cost of the softening factor is to weakly break the conservation of energy. Softening is equivalent to adding some small scale damping which is physically justified [25]. Since the softening factor is independent of direction, the violation of energy conservation should fluctuate in no particular direction around the initial energy value for large numbers of close vortex approaches. The softening factor also introduces the possibility of a vortex being pushed out of the domain of the disk. These issues make it imperative to check that all vortices remain inside the domain for the duration of the simulation and that the energy is conserved to a reasonable approximation.

6.3 Numerical model tests

Simple checks were preformed to ensure that the computational simulations corresponded with known analytic solutions of the point vortex model. First a vortex was placed close to the boundary. The velocity should be greater for a vortex close to the boundary than a vortex at a distance further away. The direction that the positive and negative charged vortices move within the domain must also agree with the model. The vortex simulation produced the expected behaviour with these simple checks.

Next the validity of the simulation was checked with the stationary solutions calculated in Chapter 5. In figure 6.1, two vortices of opposite charge were initially placed at the stationary distance d from the origin. The configuration was then simulated for $\bar{t} = 3001$ steps. The vortices remained phase locked at the stationary distance from the origin in agreement with the analytic result.

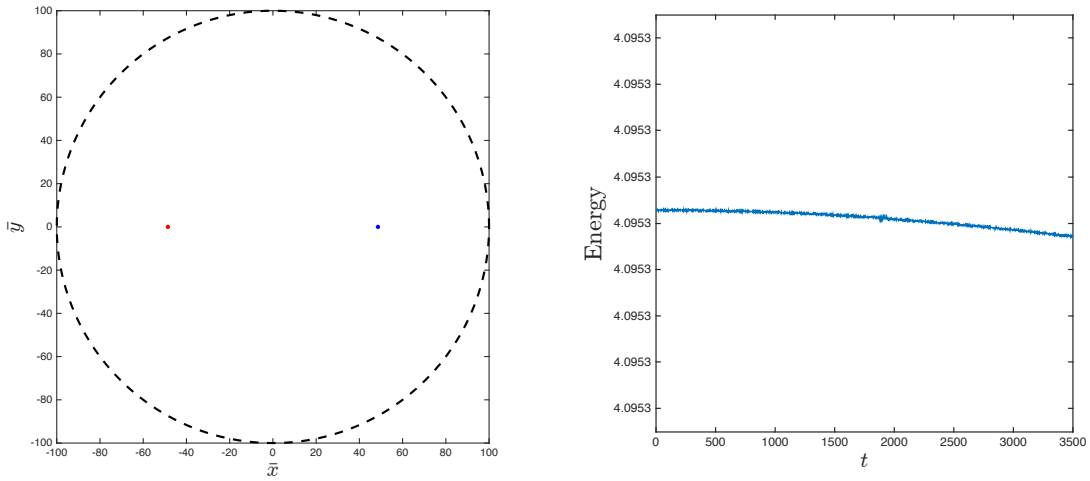

(a) Vortices at stationary Position

(b) Final State

Fig. 6.1 a) Two vortices remaining at each stationary distance d after $\bar{t} = 3,001$ steps with disk radius $\bar{R} = 100$. b) Energy versus time for the simulation in figure a) .

Checking the energy conservation is an important task to ensure the simulation working correctly. Figure 6.1b, shows the energy of the system versus time. The energy was reasonably conserved to at least 4 decimal places for the total duration of the simulation giving confidence in the result.

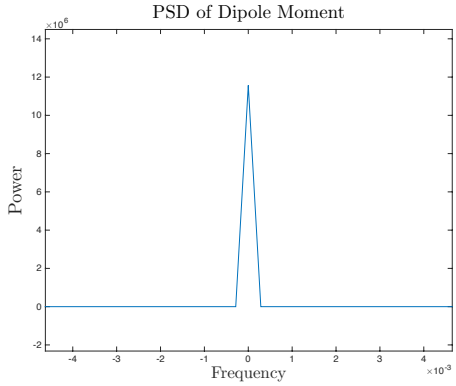

Fig. 6.2 Power spectral density plot of two vortices initially placed at the stationary points and evolved for 3001 time steps

The power spectral density of the two vortex stationary system was calculated. Figure 6.2 shows the power spectral density of the dipole moment centred around a frequency of zero, agreeing with the analytic prediction of the vortices remaining stationary.

Chapter 7

Numerical Results

7.1 Overview of results

First the trajectories of two vortices perturbed from the stationary positions is investigated. To eliminate dipolar clusters precessing around the origin two general approaches are used. This first is to create vortex clusters with zero angular momentum, and the second is to break the symmetry of the disk.

There are two methods used to create the vortex clusters with zero angular momentum. The first method is to create symmetrical circular arrangements of vortices around the stationary points or around the points of perturbation. The second method is to populate the disk with random vortices in symmetric areas around the stationary or perturbation points, and then work the arrangement into a state of low angular momentum and specific energy by a process called annealing.

7.2 Perturbation trajectories for two vortices

To check the analytic prediction for the aspect ratio of the ellipse, two vortices of opposite charge in the stationary configuration were perturbed by varying magnitudes. Figure 7.1 shows the trajectories of the vortices after perturbation by discrete magnitudes. The smallest trajectory of each vortex result from a perturbation magnitude of 1/50 of the distance from the origin to the stationary position. The largest trajectories result from a perturbation magnitude of 2/3 of the distance from the origin to the stationary point.

The aspect ratio was calculated by taking the ratio of the largest width to the largest length. Table 7.1 shows the results from perturbation by magnitude ε. The smallest perturbation gives

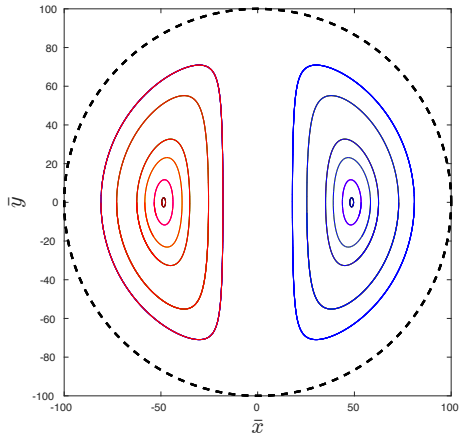

Fig. 7.1 Vortex Trajectories as magnitude of perturbation is changed

Table 7.1

ε	$\frac{d}{50}$	$\frac{d}{10}$	$\frac{d}{5}$	$\frac{d}{3.5}$	$\frac{d}{2}$	$\frac{d}{1.5}$
Aspect Ratio	2.4195	2.4155	2.4033	2.3872	2.3229	2.2512
Agreement	100%	99.83%	99.33%	98.67%	96.01%	93.04%

an exact agreement to at least 4 digits. The largest perturbation is still in good agreement, at 93.04%. The analytic prediction for the ratio was

$$\frac{l_1}{l_2} = \sqrt{1+3\varphi} \simeq 2.4195 \tag{7.1}$$

7.3 Dipolar vortex clusters at the stationary positions

To investigate the stability of a large number of vortices clustered around each stationary point, two domains were defined around each stationary point as shown in figure 7.2. The radius of each circular domain was $d/4$. The circular domains were randomly populated with vortices of the correct sign in order to create a large dipole. This method creates two clusters of vortices whose centres of mass are not perfectly at the stationary points, but as the number of vortices is increased each centre of mass approachs the stationary points by the law of large numbers.

The simulation of the dipolar clusters was run until $\bar{t} = 100,000$. Figure 7.3a shows the positions of the vortices at the final time step. The green and magenta lines trace out the history of the centre of mass for the positive and negative signed clusters respectively. The vortex clusters have spread out, but the energy of the system has been conserved. With no

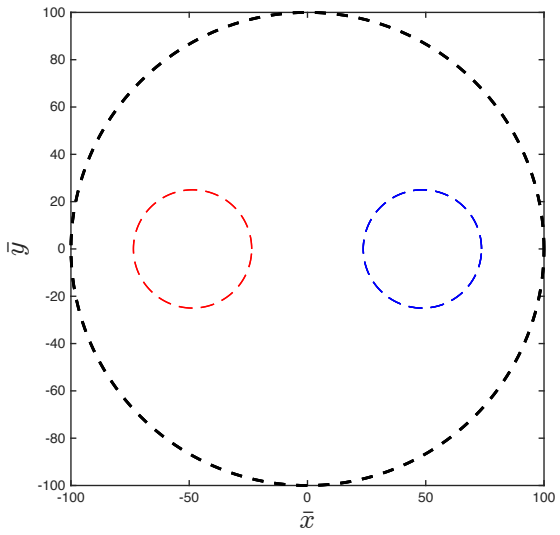

Fig. 7.2 Bounded circular domain with smaller circular domains around stationary points available to be populated by vortices. Vortices of positive sign are randomly populated inside the dashed red circle on the right while vortices of negative sign are randomly populated inside the dashed blue circle on the left.

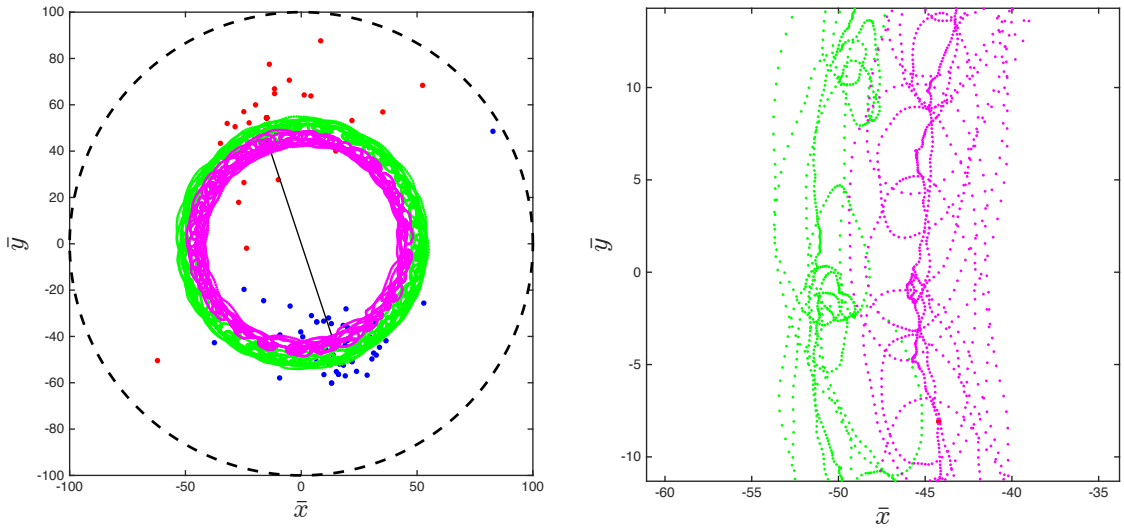

(a) (b)

Fig. 7.3 a) Two vortex clusters of opposite sign with 50 vortices each at time $\bar{t} = 100,000$. The black line represents the macroscopic dipole moment. The green and magenta lines trace out the centre of mass of each cluster through time. b) Magnification of centre of mass lines at time $\bar{t} = 100,000$. The green dots mark out the centre of mass positions of the positive vortex cluster and the magenta dots the negative vortex cluster.

defect to break the symmetry of the disk, the centre of mass of each cluster has precessed around the origin. The negatively signed vortices have precessed at a closer distance to the origin than the positively signed vortices, but this is only an artefact of the random population of vortices specific to this simulation.

Each cluster displayed a complex internal motion, but the centre of mass of each cluster did not deviate far from the stationary distance. Despite a small perturbation being built into the system due to the random population process, there does not appear to be an elliptical trajectory around the relative stationary points for each cluster. Figure 7.3b shows the centre of mass traces for each cluster in a small region of the disk. The traces appear chaotic, with no clear pattern.

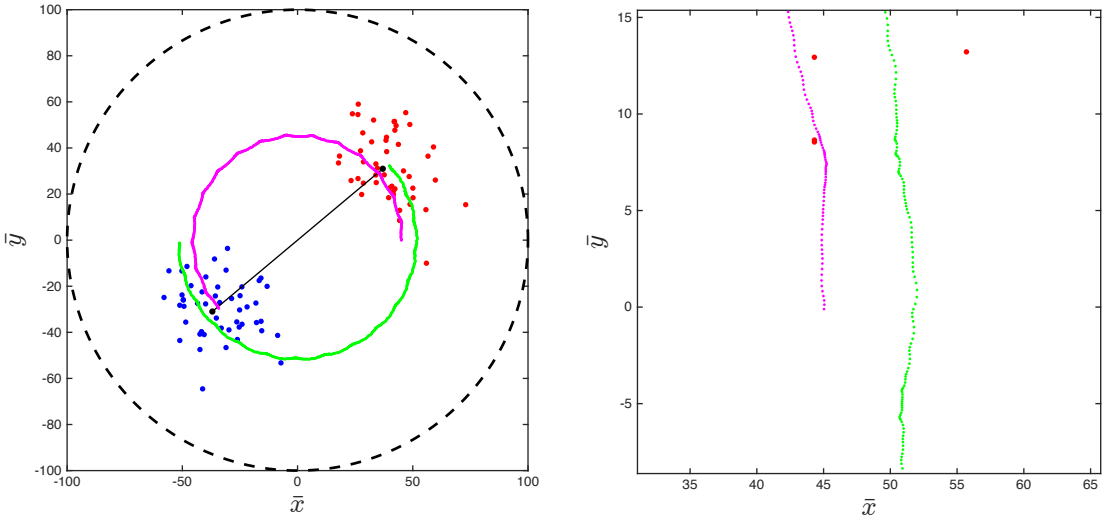

(a) (b)

Fig. 7.4 a) Two vortex clusters of opposite sign with 50 vortices each at time $\bar{t} = 10,000$. The black line represents the dipole moment. The green and magenta lines trace out the centre of mass of each cluster through time. b) Magnification of centre of mass lines at time $\bar{t} = 10,000$. The green dots mark out the centre of mass positions of the positive vortex cluster and the magenta dots the negative vortex cluster.

To investigate closer, the system is observed over different intervals of time. Figure 7.3a shows the system from $\bar{t} = 1$ to $\bar{t} = 10,000$. The clusters have not yet made an entire rotation around the origin. In figure 7.4b, the close up of the centre of mass trace lines show no elliptical trajectories, only slight variations around a circular path.

Figure 7.5a shows the system between the time intervals of $\bar{t} = 40,000$ to $\bar{t} = 50,000$. There are parts of the trajectories that are clearly elliptical. Figure 7.5b shows the trajectories clearly. There is an elliptical loop followed by a relatively straight line joining the next loop

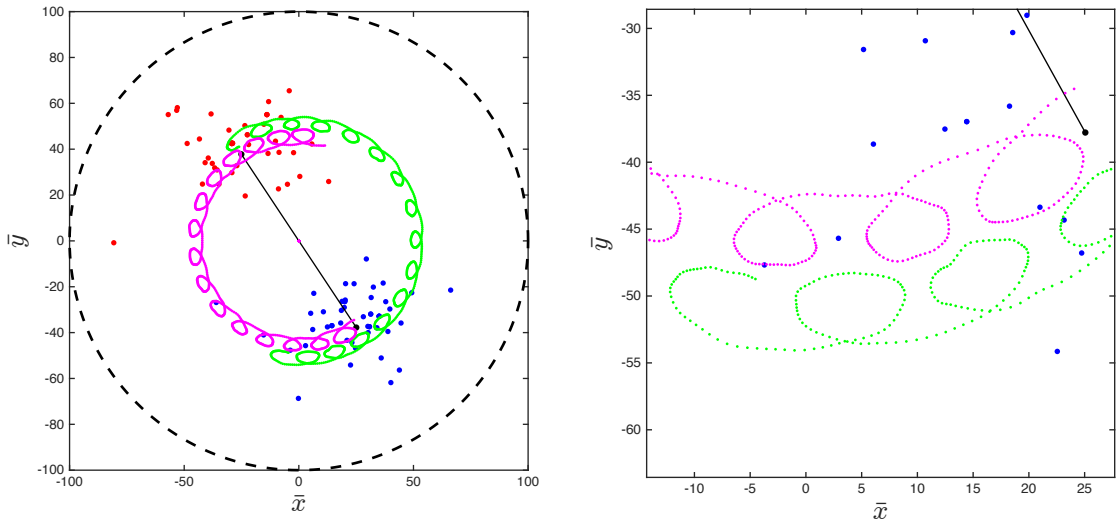

(a) (b)

Fig. 7.5 a) Two vortex clusters of opposite sign with 50 vortices each from time $\bar{t} = 40,000$ to time $\bar{t} = 50,000$. The black line represents the dipole moment. The green and magenta lines trace out the centre of mass of each cluster through time. b) Magnification of centre of mass lines from time $\bar{t} = 40,000$ to time $\bar{t} = 50,000$. The green dots mark out the centre of mass positions of the positive vortex cluster and the magenta dots the negative vortex cluster.

for each clusters centre of mass. There appears to be an elliptical loop for a cluster when the other cluster is following a relatively straight trajectory.

The last interval of time to be observed is from $\bar{t} = 90,000$ to $\bar{t} = 100,000$. Figure 7.6a shows that the centre of mass for each cluster have stopped tracing out consistent patterns in this time interval relative to the pervious time interval. The lengths and widths of the elliptical trajectories vary by a large amount. Figure 7.6b shows the upper right region of the disk, where the trajectories are clear. The motion of the positive signed cluster in this region is becoming chaotic.

Putting the whole picture together, the system starts out precessing about the origin since the centre of mass of each cluster is not precisely at the stationary points. The small deviations from the stationary points cause the precession trajectories to deviate. As the system evolves, the deviations grow and behave like a perturbation. But the analytic perturbation of two vortices perturbs both vortices by the same magnitude in opposite directions. The random effective perturbation of each cluster in this simulation leads to the chaotic trajectories. To investigate whether the trajectories will alternate between elliptical and chaotic requires a simulation over a longer period of time.

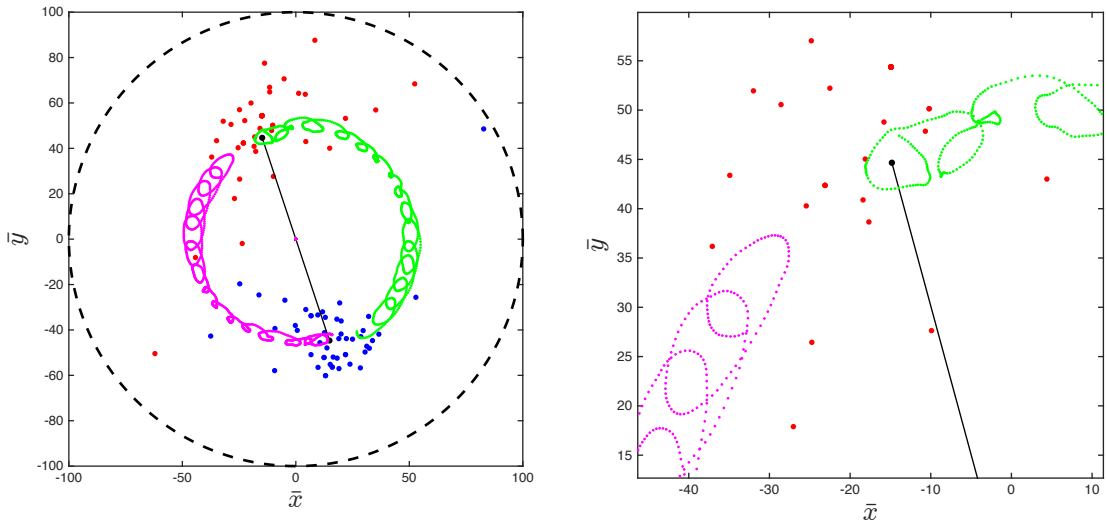

(a) (b)

Fig. 7.6 a) Two vortex clusters of opposite sign with 50 vortices each from time $\bar{t} = 90,000$ to time $\bar{t} = 100,000$. The black line represents the dipole moment. The green and magenta lines trace out the centre of mass of each cluster through time. b) Magnification of centre of mass lines from time $\bar{t} = 90,000$ to time $\bar{t} = 100,000$. The green dots mark out the centre of mass positions of the positive vortex cluster and the magenta dots the negative vortex cluster.

Despite the inability to resolve the aspect ratio for the sometimes existent elliptical trajectories of the vortex clusters, the frequency of oscillation for the clusters can be determined by examining the fluctuation spectra of the macroscopic dipole moment.

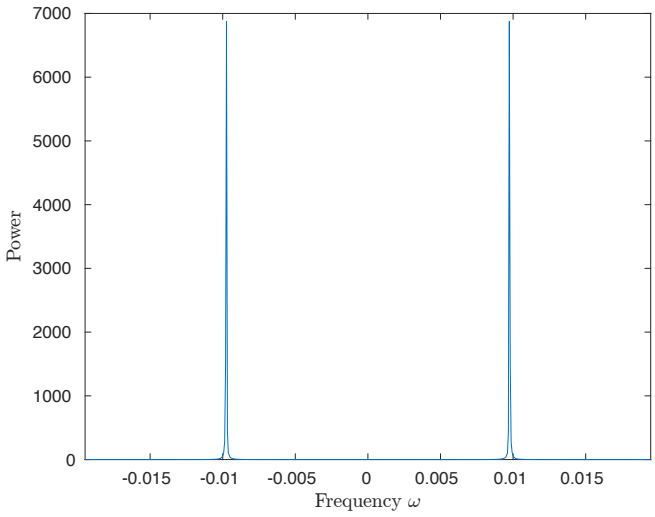

Fig. 7.7 Power spectrum of the macroscopic dipole moment for large dipolar vortex clusters at the stationary points.

Figure 7.7 shows the power spectral density of the macroscopic dipole moment. The dominant zero mode signal was removed by subtracting the mean of the macroscopic dipole moment from the macroscopic dipole moment before Fourier analysis. Two sharp and narrow peaks are centred around the numerical frequency of $\omega = \pm 0.009739$. To check this against the analytic result that was derived in Chapter 5, the numerical angular frequency must be divided by half the number of vortices in the simulation and multiplied by the non-dimensional radius of the disk squared. This is because the analytic angular frequency was calculated for two vortices, but each cluster has $N/2$ times that many vortices. The multiplication by the non-dimensional radius squared returns the result to a form easy to compare with the analytic result. For a reminder, the analytic result was

$$\omega \simeq \frac{\hbar}{mR^2} 1.9574. \tag{7.2}$$

The numerical angular frequency in comparable form is

$$\frac{0.009739}{50} R^2 = 1.9478 \tag{7.3}$$

This result is in strong agreement with the analytic prediction of angular frequency about the stationary positions, despite the trajectories of the centre of masses behaving erratically.

7.4 Perturbed dipolar vortex clusters

By using the dipolar vortex cluster generating process from the previous section, but shifting the centre of both circular domains by a distance $\varepsilon = \frac{d}{10}$ away from the origin, the perturbation of two large dipolar clusters can be investigated. Figure 7.8a shows the simulation from time $\bar{t} = 1$ to time $\bar{t} = 3,000$. The green and magenta lines trace out the history of the centre of mass for the positive and negative signed clusters respectively. Figure 7.8b shows the traces are elliptical as they precess about the origin. An effective algorithm to calculate the average aspect ratio of these elliptical trajectories has not yet been implemented. The fluctuation spectra of the macroscopic dipole moment gives an angular frequency of

$$\frac{0.0095505}{50} R^2 = 1.9101 \tag{7.4}$$

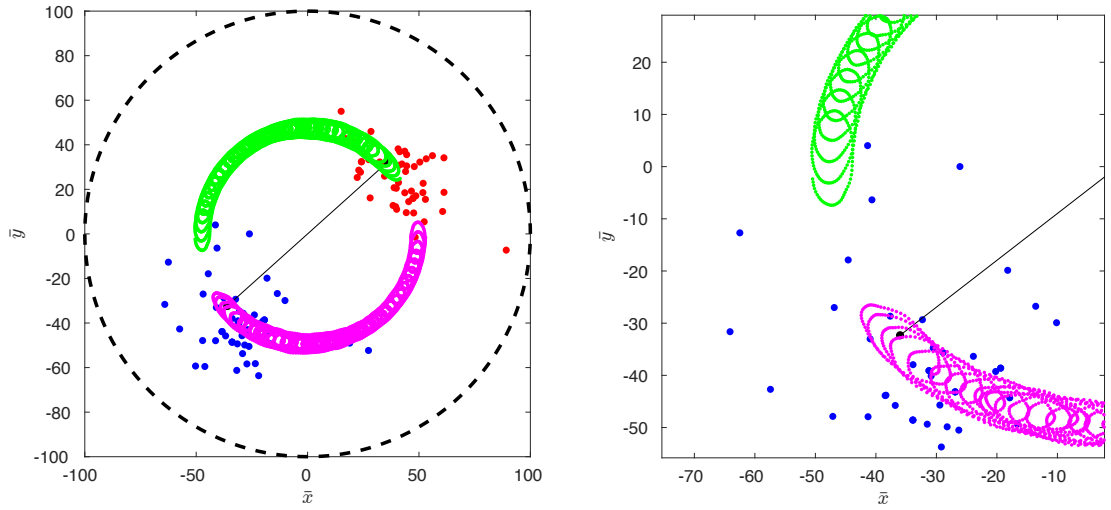

(a) (b)

Fig. 7.8 a) Two vortex clusters of opposite sign with 50 vortices each from time $\bar{t} = 1$ to time $\bar{t} = 3,000$. The black line represents the dipole moment. The green and magenta lines trace out the centre of mass of each cluster through time. b) Magnification of centre of mass lines from time $\bar{t} = 1$ to time $\bar{t} = 3,000$. The green dots mark out the centre of mass positions of the positive vortex cluster and the magenta dots the negative vortex cluster.

a 97.5% agreement with the analytic result. Clearly the perturbation of two dipolar vortex clusters comprised of N vortices behaves like the perturbation of two vortices of charge $N/2$.

7.5 Symmetric zero angular momentum states

To eliminate the precession of the dipolar vortex clusters about the origin, symmetric circular rings of vortices were created around each stationary point such that there was no net angular momentum. The distance between the circular rings can be scaled so that the energy of the system can be varied. A smaller distance between vortices of like sign increases the energy of the system. In each simulation in this section, there were 24 vortices in total, with 12 vortices of positive sign around the stationary point to the right, and 12 vortices of negative sign around the station point to the left.

The scale of the distance between the circular rings of vortices were chosen to create energy states starting from $\bar{E} = 60$ down to $\bar{E} = 10$ with steps of $\bar{E} = 5$ in between. Figure 7.9 shows these initial states. The highest energy states are very dense, almost point like. In order to probe the behaviour of the system at lower energies, the circular arrangement can not be used because scaling the circular rings further would place vortices outside of the disk.

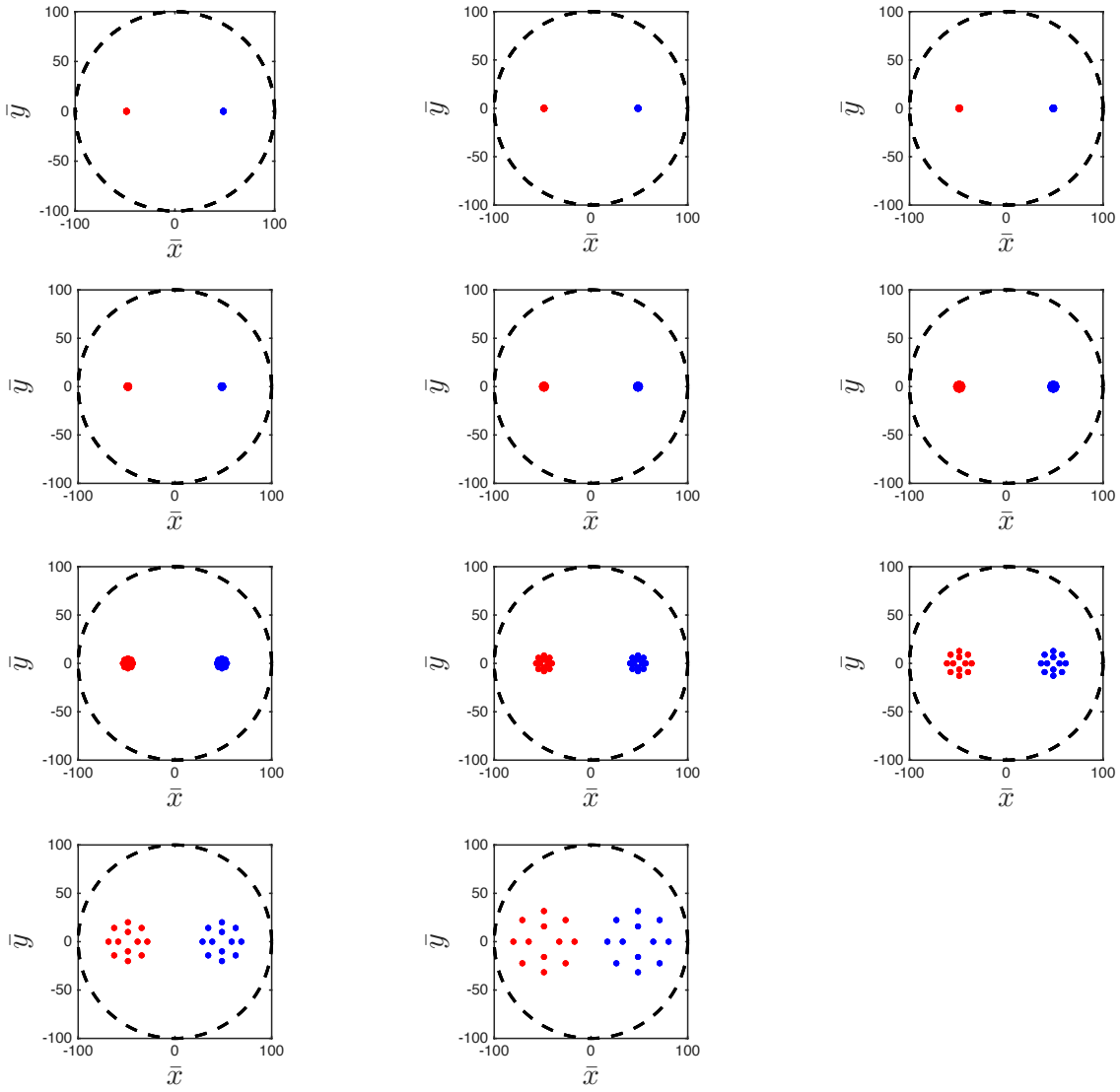

Fig. 7.9 Initial symmetric circular vortex states. Top row from left to right shows initial energy of 60, 55, 50, The second row shows 45, 40, 35, third row 30, 25, 20 and the last row shows 15, 10

Each simulation was run until $\bar{t} = 100,000$. The fluctuation spectra of the dipole moment was calculated for each energy state. In order to remove the dominant zero mode signal from the fluctuation spectra, the mean of the macroscopic dipole moment was subtracted. To investigate how the system diverges from the analytic results as the energy is changed, the widths of the spectrum around the dipole frequency peaks were measured.

Table 7.2 shows the results of the spectral analysis of the macroscopic dipole moment. The frequencies have again been converted into a form for easy comparison with the analytic result, by diving by $N/2$ and multiplying by the non-dimensional radius squared. The high

Table 7.2 Circular Symmetric States

Energy	Dipole Frequency	Analytic Agreement	FWHM
60	1.9375	98.98%	0.8713
55	1.9375	98.98%	0.8689
50	1.9375	98.98%	0.8689
45	1.9375	98.98%	0.7064
40	1.9375	98.98%	0.7418
35	1.9375	98.98%	0.7678
30	1.9375	98.98%	1.364
25	1.9900	98.33%	1.007
20	2.0417	95.69%	2.715
15	1.9375	98.98%	2.041
10	1.6758	85.61%	1.052

energy states give a consistent frequency value in close agreement with the analytic result. The lower energy states diverge from this result, with some states giving a higher frequency than the analytic result and others a lower frequency.

The full width half maximums of the dipole frequency peaks were calculated by fitting a Gaussian over the peaks and using the relation

$$FWHM = 2\sqrt{2\ln 2}\sigma, \tag{7.5}$$

where σ is the standard deviation of the Gaussian fit. The high energy states have a constrained width, while the low energy states have divergent widths.

To get a better sense of what is going on in the system, we compare the spectra and final states of the system at the lowest energy $\bar{E} = 10$ and the highest energy $\bar{E} = 60$. Figure 7.10a shows the power spectrum for the system with energy $\bar{E} = 10$. The red line marks the analytic result for the dipole frequency. The spectrum around the dipole frequency is made up of three large peaks of varying power, with smaller oscillations about them. This is in contrast to the power spectrum for the system with energy $\bar{E} = 60$ shown in figure 7.11a, where the there is a narrow and sharp peak about the dipole signal, with the dashed red line marking the analytic signal that is in very close agreement.

Figure 7.10b shows the final state of the system with energy $\bar{E} = 10$ at $\bar{t} = 100,000$. The vortices have spread out into a non symmetrical arrangement, with the centre of mass of

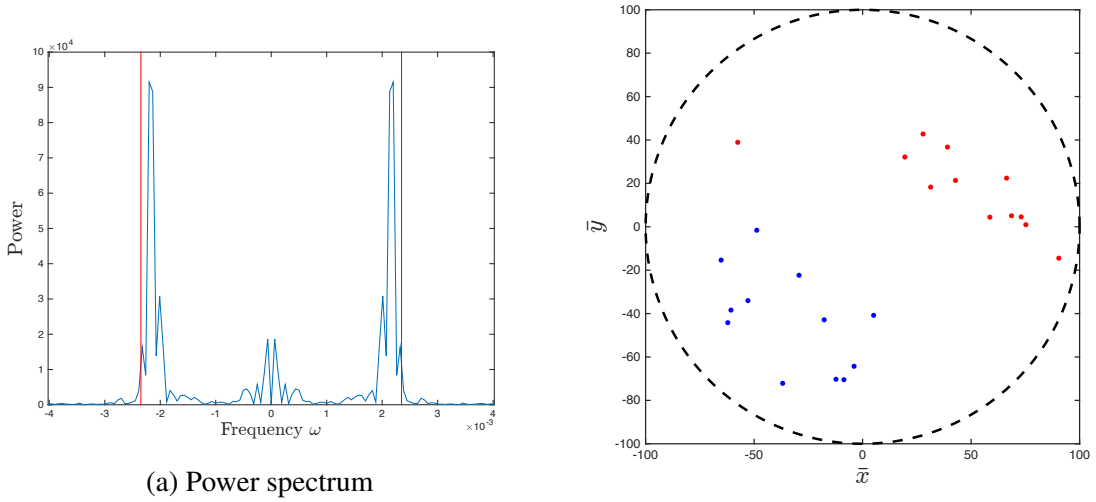

(a) Power spectrum

(b) Final state

Fig. 7.10 Power spectrum of the macroscopic dipole moment and final state of simulation for system with energy 10. The red lines show the analytic frequency.

each cluster having precessed around the origin. Figure 7.11b shows the circular vortex state with energy $\bar{E} = 60$ at $\bar{t} = 100,000$. The vortices have maintained their dense symmetrical arrangement.

In summary, the lower energies evolve into chaotic states, while the high energy states maintain their symmetric form. These dense symmetric arrangements act as if each cluster were vortex of charge N/2, where N is the number of vortices in the arrangement. Despite no precession around the stationary point, the fluctuation spectra still gives a small angular frequency signal mostly clearly seen in the power spectrum of the lowest energy state. To see precession around the origin the system by the highest energy state would require the system to be evolved for a longer period of time.

7.6 Annealed zero angular momentum states

In order to create dipolar vortex clusters with lower energy and that are more likely to occur physically, an annealing process is applied to the result of vortices being randomly populated inside the smaller circular domains. The annealing process randomly selects a vortex. It then generates a new random position for the vortex within the domain of the disk. If the new location lowers the angular momentum and moves towards the desired energy value, the the new location is accepted and the annealing process selects another vortex and repeats until the required angular momentum and energy level conditions are met to within a given

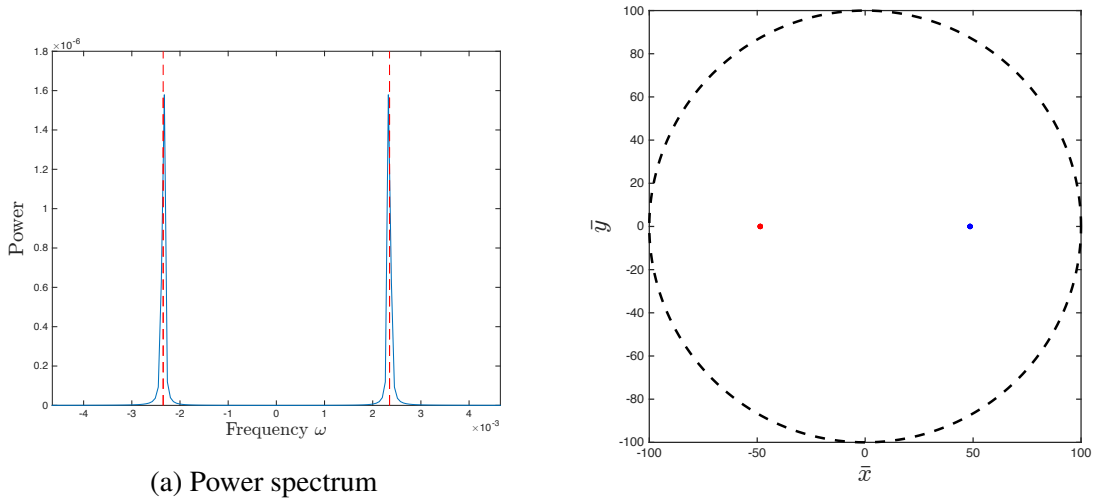

(a) Power spectrum

(b) Final state

Fig. 7.11 Power spectrum of the macroscopic dipole moment and final state of simulation for system with energy $\bar{E} = 60$. The red lines show the analytic frequency.

tolerance. The tolerance for the energy values was $\bar{E} = \pm 0.1$ of the target value, and the tolerance for the angular momentum was $\bar{L} = \pm 1 \times 10^{-4}$.

The initial zero angular momentum states that were generated by this annealing process are shown in Figure 7.12. The top row from left to right has an energy of $\bar{E} = 45$, $\bar{E} = 40$ and $\bar{E} = 35$. The middle row has energies of $\bar{E} = 30$, $\bar{E} = 25$ and $\bar{E} = 20$ and the bottom row has energies of $\bar{E} = 15$, $\bar{E} = 10$ and $\bar{E} = 5$. By positioning positive and negative vortices together, the annealing process can reduce the energy of the system.

The spectra of the macroscopic dipole momentum for each energy was calculated, with the mean of the macroscopic dipole moment subtracted from the macroscopic dipole moment before Fourier analysis. Figure 7.13 shows the power spectral density of the annealed states from highest energy to lowest. The x axis has been limited to show only the parts of the spectrum with any significant signal. At high energy, there is a strong dipole signal. There is also a large very low frequency centred around zero.

Table 7.3 shows the dipole frequency for the annealed energy states. The high energy states give a reasonable agreement with the analytic frequency prediction. A curve was fit to the dipole frequency for each energy state and the divergence from the analytic prediction but the relationship between the two variables while following a trend is stochastic. The full width half maximum could not be calculated, as the peaks in the power spectrum were no longer clearly defined, due to line broadening with several peaks contributing around the dipole frequency.

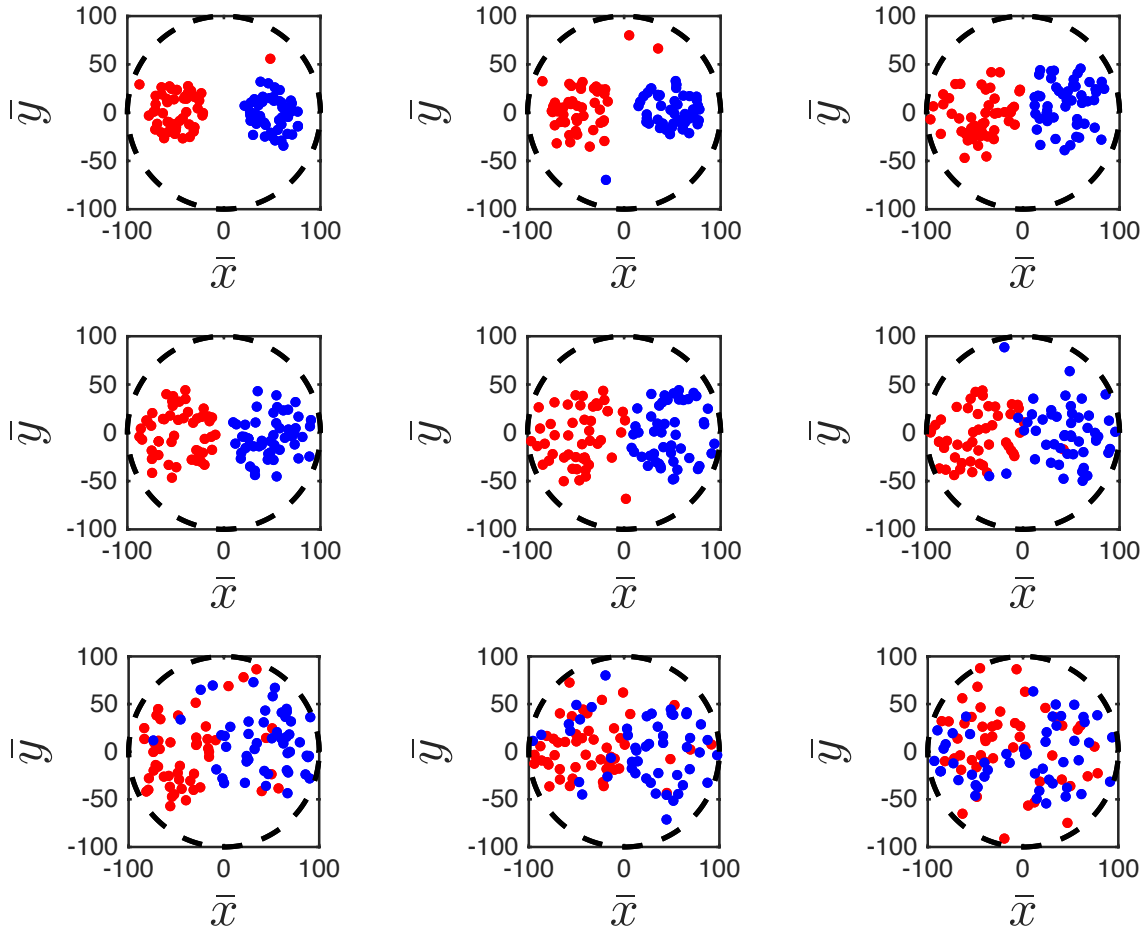

Fig. 7.12 Initial annealed zero angular momentum vortex states. The top row from left to right has an energy of $\bar{E} = 45$, $\bar{E} = 40$ and $\bar{E} = 35$. The middle row has energies of $\bar{E} = 30$, $\bar{E} = 25$ and $\bar{E} = 20$ and the bottom row has energies of $\bar{E} = 15$, $\bar{E} = 10$ and $\bar{E} = 5$.

As part of the checks that are done for each result, an anomaly appeared for the lowest energy state. Figure 7.14 shows the angular momentum versus time for each of the annealed zero angular momentum energy states. The angular momentum is not perfectly conserved for any states, but for the systems with initial energy $\bar{E} = 45$ down to $\bar{E} = 10$ it is approximately conserved. The lowest energy system, $\bar{E} = 5$ has a divergent angular momentum at $\bar{t} = 2343$. By investigating the error, it was found that the softening factor had placed some vortices outside the boundary of the disk.

Three more attempts were made to simulate the $\bar{E} = 5$ state. The annealing process was repeated and inspected for any anomalies. The generated state was then run with a reduced softening factor of 1×10^{-5}, but vortices continued to be pushed across the boundary. The softening factor was reduced by an order of magnitude again, but the problem persisted.

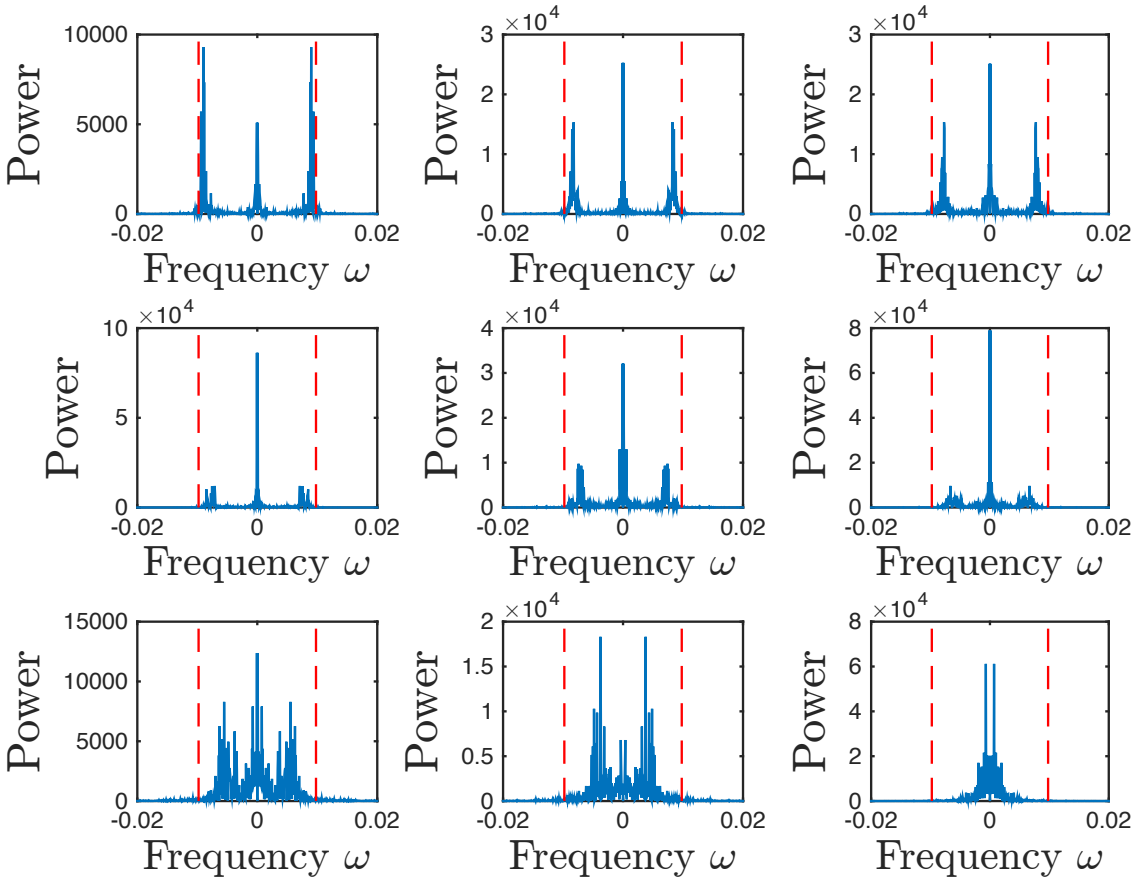

Fig. 7.13 Power spectral density of the macroscopic dipole moment for the zero angular momentum annealed energy states. The top row from left to right has an energy of $\bar{E} = 45$, $\bar{E} = 40$ and $\bar{E} = 35$. The middle row has energies of $\bar{E} = 30$, $\bar{E} = 25$ and $\bar{E} = 20$ and the bottom row has energies of $\bar{E} = 15$, $\bar{E} = 10$ and $\bar{E} = 5$.

Finally, the softening factor was removed, but the computation halted as the integration routines tolerances could not be met. These issues make the results from the $\bar{E} = 5$ states invalid. To proceed to simulate lower energy states with high vortex numbers, the introduction of boundary and vortex-antivortex pair annihilation may need to be introduced.

Table 7.3 Annealed zero angular momentum states

Energy	Dipole Frequency	Analytic Agreement
45	1.7970	91.81%
40	1.6462	84.10%
35	1.5456	78.96%
30	1.5080	77.04%
25	1.4828	75.75%
20	1.3320	68.05%
15	1.1058	56.49%
10	0.7540	38.52%
5	0.3896	19.90%

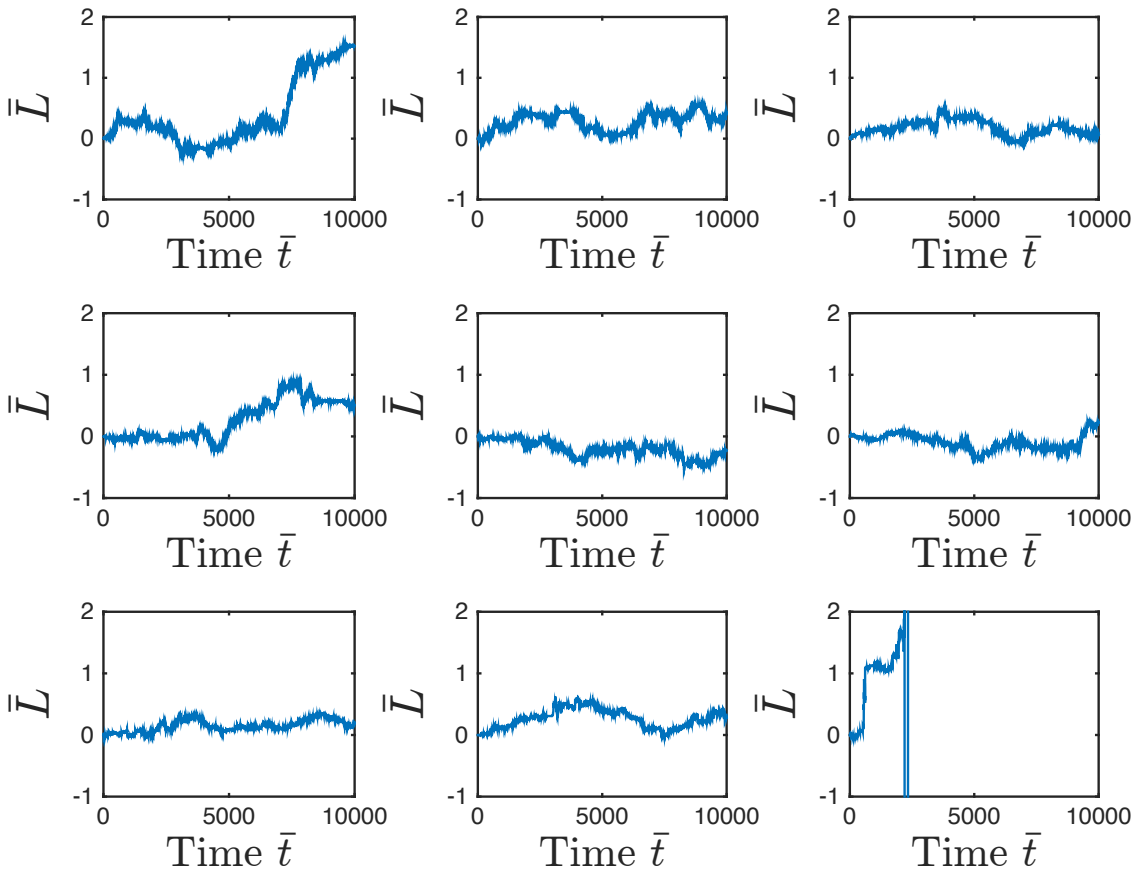

Fig. 7.14 Angular momentum versus time. The top row from left to right has an energy of $\bar{E} = 45$, $\bar{E} = 40$ and $\bar{E} = 35$. The middle row has energies of $\bar{E} = 30$, $\bar{E} = 25$ and $\bar{E} = 20$ and the bottom row has energies of $\bar{E} = 15$, $\bar{E} = 10$ and $\bar{E} = 5$. The lowest energy state clearly diverges.

Chapter 8

Conclusion

8.1 Concluding Remarks

The motivation for this study came from the experiment at the University of Queensland [8]. The physical experiment was a complex condensed matter system with diverse physical features, many of which are very challenging to model. We choose to focus on the characteristics of the macroscopic vortex dipole fluctuations in the superfluid helium II believing they were relevant to the experiment.

We found that for high energy dipolar clusters, the dominant source of fluctuations stems from fluctuations of the macroscopic dipole moment. We calculated the frequency of this mode analytically and found good agreement with our numerical results over a broad range of energies, particularly at the high energy limit. A systematic study of the relationship between the macroscopic dipole moment and the energy of the system was presented, with the line broadening of the spectrum also explored.

Given that the fluctuations of the macroscopic dipole moment may couple to the phonon modes of the mechanical oscillator and optical modes of the evanescent optical field, we hope to tie these results to the motivating experiment in the near future. An explanation of the work that is continuing is briefly discussed in appendix A.

The analytic results derived in this project have broader applications than the motivating experiment. Clusters of vortices can be produced in BEC's [26] and recent work in systems with negative temperatures in confined two-dimensional quantum fluids produce clusters of high energy vortices in similar form to the work presented here [27].

References

[1] K. Masuda and M. Nitta, "Magnetic properties of quantized vortices in neutron $^3p_2$ superfluids in neutron stars," *Phys. Rev. C*, vol. 93, p. 035804, Mar 2016.

[2] P. Hanlon, "New twist on turbulence," *Nat Phys*, aug 2005.

[3] M. W. Zwierlein, J. R. Abo-Shaeer, A. Schirotzek, C. H. Schunck, and W. Ketterle, "Vortices and superfluidity in a strongly interacting fermi gas," *Nature*, vol. 435, pp. 1047–1051, jun 2005.

[4] H. E. Hall and W. F. Vinen, "The rotation of liquid helium II. II. the theory of mutual friction in uniformly rotating helium II," *Proceedings of the Royal Society A: Mathematical, Physical and Engineering Sciences*, vol. 238, pp. 215–234, dec 1956.

[5] L. Onsager, "Statistical hydrodynamics," *Il Nuovo Cimento (1943-1954)*, vol. 6, no. 2, pp. 279–287, 1949.

[6] G. I. Harris, D. L. McAuslan, E. Sheridan, Y. Sachkou, C. Baker, and W. P. Bowen, "Laser cooling and control of excitations in superfluid helium," *Nat Phys*, vol. advance online publication, Apr 2016. Article.

[7] D. K. Armani, T. J. Kippenberg, S. M. Spillane, and K. J. Vahala, "Ultra-high-q toroid microcavity on a chip," *Nature*, vol. 421, pp. 925–928, Feb 2003.

[8] D. L. McAuslan, G. I. Harris, C. Baker, Y. Sachkou, X. He, E. Sheridan, and W. P. Bowen, "Microphotonic forces from superfluid flow," *Phys. Rev. X*, vol. 6, p. 021012, Apr 2016.

[9] M. Aspelmeyer, T. J. Kippenberg, and F. Marquardt, "Cavity optomechanics," *Rev. Mod. Phys.*, vol. 86, pp. 1391–1452, Dec. 2014.

[10] M. Aspelmeyer, T. J. Kippenberg, and F. Marquardt, "Cavity optomechanics," *Rev. Mod. Phys.*, vol. 86, pp. 1391–1452, Dec 2014.

[11] C. V. Raman, "A new radiation," *Indian J. Phys.*, vol. 2, pp. 387–398, 1928.

[12] A. Kitai, *Luminescent Materials and Applications*. Wiley Series in Materials for Electronic & Optoelectronic Applications, Wiley, 2008.

[13] T. J. Kippenberg, H. Rokhsari, T. Carmon, A. Scherer, and K. J. Vahala, "Analysis of radiation-pressure induced mechanical oscillation of an optical microcavity," *Phys. Rev. Lett.*, vol. 95, p. 033901, Jul 2005.

[14] C. A. Hampel, *The Encyclopedia of the Chemical Elements*. Van Nostrand Reinhold, 1968.

[15] L. D. Landau, "The theory of superfluidity of helium ii," *J. Phys. (USSR)*, vol. 5, 1941.

[16] L. Landau and E. Lifshitz, *Fluid Mechanics*. No. v. 6, Elsevier Science, 2013.

[17] R. Donnelly, *Quantized Vortices in Helium II*. No. v. 2 in Cambridge Studies in American Literature and Culture, Cambridge University Press, 1991.

[18] K. R. Atkins, "Third and fourth sound in liquid helium ii," *Phys. Rev.*, vol. 113, pp. 962–965, Feb 1959.

[19] L. Tisza, "The theory of liquid helium," *Phys. Rev.*, vol. 72, pp. 838–854, Nov 1947.

[20] E. Madelung, "Eine anschauliche deutung der gleichung von schrödinger," *Naturwissenschaften*, vol. 14, no. 45, pp. 1004–1004, 1926.

[21] Private communication with W. P. Bowen, 2016.

[22] H. Aref, "Point vortex dynamics: A classical mathematics playground," *Journal of Mathematical Physics*, vol. 48, no. 6, 2007.

[23] G. Kirchhoff and W. Wien, *Vorlesungen über mechanik*. Vorlesungen uber mathematischephysik, B. G. Teubner, 1897.

[24] H. Helmholtz, "Uber integrale der hydrodynamischen gleichungen, welche den wirbelbewegungen entsprechen," *J. Reine Angew. Math*, vol. 55, pp. 25–55, 1858.

[25] T. P. Billam, M. T. Reeves, and A. S. Bradley, "Spectral energy transport in two-dimensional quantum vortex dynamics," *Phys. Rev. A*, vol. 91, p. 023615, Feb 2015.

[26] S. Middelkamp, P. Kevrekidis, D. Frantzeskakis, R. Carretero-González, and P. Schmelcher, "Emergence and stability of vortex clusters in bose–einstein condensates: A bifurcation approach near the linear limit," *Physica D: Nonlinear Phenomena*, vol. 240, no. 18, pp. 1449 – 1459, 2011.

[27] X. Yu, T. P. Billam, J. Nian, M. T. Reeves, and A. S. Bradley, "Theory of the vortex-clustering transition in a confined two-dimensional quantum fluid," *Phys. Rev. A*, vol. 94, p. 023602, Aug 2016.

[28] O. K. Pashaev and O. Yilmaz, "Vortex images and q -elementary functions," *Journal of Physics A: Mathematical and Theoretical*, vol. 41, no. 13, p. 135207, 2008.

[29] D. Crowdy and J. Marshall, "Analytical formulae for the kirchhoff–routh path function in multiply connected domains," *Proceedings of the Royal Society of London A: Mathematical, Physical and Engineering Sciences*, vol. 461, no. 2060, pp. 2477–2501, 2005.

Appendix A

Work in progress

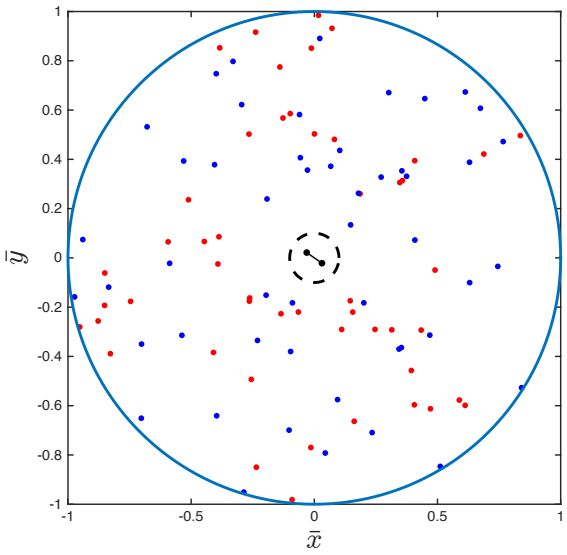

Fig. A.1 Vortices in an annular domain.

To better approximate the physical system, work has begun to put a cylindrical defect into the simulations. A paper by P.K. Oktay outlines the process to derive the hamiltonian and equations of motion of vortices in the annular domain [28]. As shown in figure A.1, the simulations for vortices in an annular domain are currently working. The point vortex model in the annular domain requires the use of Q-calculus to specify the infinite set of image charges. The numerical implementation uses a truncated form of the full equations of motion.

The Hamiltonian for the annular domain may not be able to be manipulated to move the inner cylinder from the origin to another position to mimic the defect. If the Hamiltonian for the annular domain can not be modified, a paper by D. Crowdy [29] contains the formalism

for point vortices inside multiply the connected domain. The formalism is mathematically complicated, but can be used to derive the specific solution for an inner cylinder inside the circular domain to mimic the defect.